A Four-Coordinate End-On Superoxocopper(II) Complex: Probing the Link Between Coordination Number and Reactivity.

Suman Debnath,[a,‡] Shoba Laxmi,[a,‡] Olivia McCubbin Stepanic,[b] Sebastian Y. Quek,[a] Maurice van Gastel,[c] Serena DeBeer,[b,*] Tobias Krämer,[d,e,*] and Jason England.[a,f,*]

[a] Division of Chemistry and Biological Chemistry, School of Chemistry, Chemical Engineering and Biotechnology, Nanyang Technological University, 21 Nanyang Link, Singapore 637371.

[b] Max Planck Institute for Chemical Energy Conversion, Stiftstr. 34 – 36, Mülheim an der Ruhr, D-45470, Germany.

[c] Max-Planck-Institut für Kohlenforschung, Kaiser-Wilhelm-Platz, Mülheim an der Ruhr, D-45470, Germany.

[d] Department of Chemistry, Maynooth University, Maynooth, Co. Kildare, Ireland.

[e] Hamilton Institute, Maynooth University, Maynooth, Co. Kildare, Ireland.

[f] School of Chemistry, University of Lincoln, Lincoln, LN6 7TW, U.K.

ABSTRACT: Comparison of the substrate reactivity of four- versus five-coordinate end-on superoxocopper(II) complexes is complicated by the relative scarcity of the former and the difference in donor atoms that have been used to support these two geometries. Herein, we report a four-coordinate end-on superoxocopper(II) complex supported by a sterically encumbered bis(2-pyridylmethyl)amine ligand, dpb$_2$-^{Me}BPA (**1**), and comparison of its substrate reactivity with that of a five-coordinate end-on superoxocopper(II) complex ligated by a similarly substituted tris(2-pyridylmethyl)amine, dpb$_3$-TMPA (**2**). These ligands differ by the presence/absence of a single pyridine donor. Kinetic isotope effect (KIE) measurements and correlation of second order rate constants (k_2's) versus oxidation potentials (E_{ox}) for a range of phenols indicates that the complex [Cu^{II}(η^1-O$_2^{\bullet-}$)(**1**)]$^+$ reacts with phenols via a similar hydrogen atom transfer (HAT) mechanism as [Cu^{II}(η^1-O$_2^{\bullet-}$)(**2**)]$^+$. However, [Cu^{II}(η^1-O$_2^{\bullet-}$)(**1**)]$^+$ performs HAT much more quickly, with its k_2 for reaction with 2,4-di-tert-butyl-4-methoxyphenol (MeO-ArOH) being > 100 times greater. Furthermore, [Cu^{II}(η^1-O$_2^{\bullet-}$)(**1**)]$^+$ can oxidize C-H bond substrates possessing stronger bonds than [Cu^{II}(η^1-O$_2^{\bullet-}$)(**2**)]$^+$, and it reacts with *N*-methyl-9,10-dihydroacridine (^{Me}AcrH) approximately 200 times faster. The much greater facility for substrate oxidation displayed by [Cu^{II}(η^1-O$_2^{\bullet-}$)(**1**)]$^+$ is attributed to its more open coordination sphere, which allows easier substrate approach than [Cu^{II}(η^1-O$_2^{\bullet-}$)(**2**)]$^+$. These observations are of relevance to enzymes in which four-coordinate end-on superoxocopper(II) intermediates, rather than five-coordinate congeners, are routinely invoked as the active oxidants responsible for substrate oxidation.

INTRODUCTION

Mononuclear end-on superoxocopper(II) species, Cu^{II}(η^1-O$_2^{\bullet-}$), have been invoked as H-atom abstracting agents in a plethora of O$_2$ activating copper enzymes.[1, 2] This includes the non-coupled binuclear copper enzymes PHM, DβM and TβM, which catalyze hydroxylation of activated C-H bonds of their native substrates,[3] and formylglycine generating enzyme (FGE), which is responsible for the conversion of cysteine to formylglycine.[4] Although the O$_2$ activating sites in these two sets of enzymes are distinct, they are both widely believed to form 4-coordinate Cu^{II}(η^1-O$_2^{\bullet-}$) active oxidants. In the case of FGE, the supporting ligands are three cysteinate donors, one of which is the substrate and the other two are active site residues.[5-8] In contrast, the non-coupled binuclear copper monooxygenases possess active sites containing two separate Cu binding sites that are separated by about 11 Å.[9] Both contain a single Cu ion, with one (Cu$_M$) being responsible for O$_2$ activation and substrate oxidation and the other (Cu$_H$) acting solely as an electron transfer site.[10, 11] The Cu$_M$ site is ligated by 2His/1Met amino acid residues, whereas Cu$_H$ is coordinated by 3His donors. Strong support for the intermediacy of a Cu^{II}(η^1-O$_2^{\bullet-}$) species and the proposed behavior of this family of enzymes was provided by measurement of an (albeit photoreduced) X-ray crystal structure of an end-on O$_2$ adduct in PHM.[12] It revealed a Cu(η^1-O$_2$) species (in site Cu$_M$) possessing a 4-coordinate geometry that is best described as tetrahedral. In contrast, a recent neutron crystal structure of a lytic polysaccharide monooxygenase (LPMO), which catalyzes oxidative breakdown of recalcitrant polysaccharides, revealed an active site containing a mixture of 5-coordinate Cu^{II}(η^1-O$_2^{\bullet-}$) and hydroperoxocopper(II) species (relative partial occupancies of 0.30 and 0.70, respectively).[13] However, general consensus is that oxylcopper(II) or hydroxocopper(III) species are the active oxidants in LPMOs, and recent studies conclude that they are, in fact, peroxygenases, rather than oxygenases.[14-20] Thus, the Cu^{II}(η^1-O$_2^{\bullet-}$) intermediates observed in these enzymes do not react directly with substrate and, instead, they are most likely formed during off-pathway reduction of O$_2$ to H$_2$O$_2$.

The vast majority of synthetic Cu^{II}(η^1-O$_2^{\bullet-}$) model complexes published, thus far, are supported by tetradentate ligands and possess 5-coordinate geometries.[21-23] This leaves the copper centres coordinatively saturated and restricts the O$_2$-derived ligand to end-on binding. Ligands of lower denticity

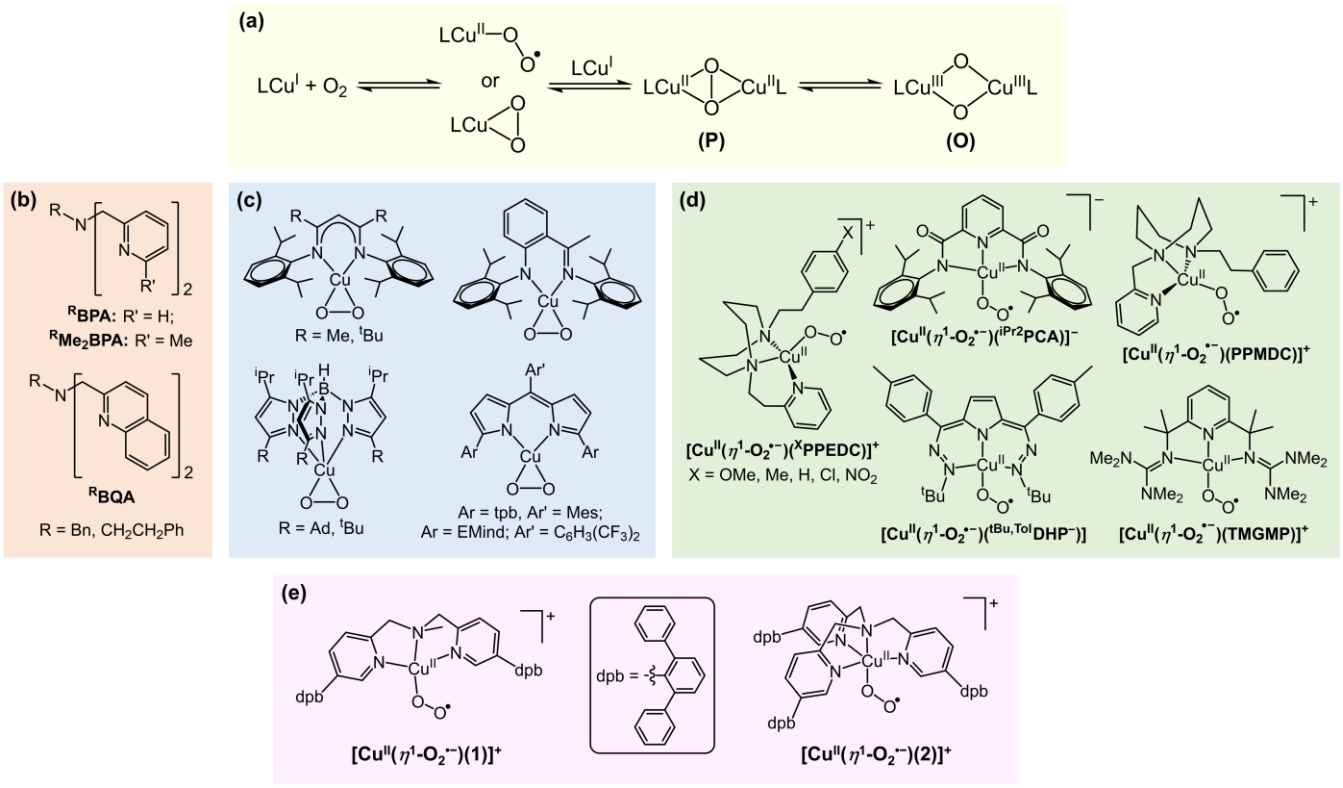

Chart 1. (a) General scheme for reaction of low-coordination number copper(I) complexes with O_2 and **(b)** published BPA-derived ligands that support this chemistry. Previously reported examples of low-coordinate **(c)** side-on (η^2) and **(d)** end-on (η^1) 1:1 adducts of copper complex and O_2. **(e)** The Cu^{II}(η^1-O$_2^{\bullet-}$) complexes studied in this work.

usually yield μ-η^2:η^2-peroxodicopper(II), Cu^{II}(μ-η^2:η^2-O$_2^{2-}$)Cu^{II} (**P**), and/or bis(μ-oxo)dicopper(III), Cu^{III}(μ-O^{2-})$_2$Cu^{III} (**O**), complexes (Chart 1a). These two species are in equilibrium with one another, and small changes in supporting ligand can lead to a shift in predominance of one over the other. This is exemplified by the tridentate *N*,*N*-bis(2-pyridylmethyl)amine (BPA) ligand framework bearing methyl, benzyl and phenylethyl substituents on the tertiary amine *N*-atom (Chart 1b).[24]

When the pyridine rings of BPA are unsubstituted (i.e., ^{R}BPA, with R' = H), an **O** species is exclusively formed.[25-27] Introduction of 6-methyl substituents (^{R}Me$_2$BPA) shifts the equilibrium almost completely to a **P** core.[28] Use of a combination of a slightly smaller 6-substituents, by replacement of the pyridyl rings with quinolyl donors, and a *N*-benzyl substituent (^{Bn}BQA) gives a clear mixture of **O** and **P** species.[29] Remarkably, the corresponding ligand bearing a slightly larger *N*-ethylbenzene substituent (^{Phe}BQA) forms only **P**.[29] In essence, introduction of steric bulk onto the BPA moiety favors formation of **P**. This has been attributed to steric inhibition of the close approach of the copper ions, which is required in formation of the **O** core. Thus far, no mononuclear O_2 adducts have been observed in these BPA complexes. However, kinetic data suggests that **O** and **P** are formed by preequilibrium binding of O_2 to a copper(I) BPA complex, to give either a Cu^{II}(η^1-O$_2^{\bullet-}$) or Cu^{II}(η^2-O$_2^{\bullet-}$) complex, followed by rate-determining reaction with a second copper(I) centre.[25, 29, 30]

Inclusion of bulky substituents onto bidentate and tridentate ligands can be used to inhibit formation of dicopper-O_2 adducts.[31-36] However, in this scenario, side-on coordination to yield either η^2-superoxocopper(II) or, in the case of more strongly reducing ligands, η^2-peroxocopper(III) complexes is commonly observed (Chart 1c).[37] This binding mode retards reactivity, which has allowed several of these complexes to be crystallographically characterized.[31, 34-36, 38] All exceptions to this side-on O_2 binding preference reported, thus far, were obtained using linear tridentate ligands (Chart 1d).[39-43] These Cu^{II}(η^1-O$_2^{\bullet-}$) complexes display a number of common structural and spectroscopic features, but they exhibit very different reactivity properties.

Tolman's and Anderson's 4-coordinate complexes [Cu^{II}(η^1-O$_2^{\bullet-}$)(^{iPr2}PCA)]$^-$ and [Cu^{II}(η^1-O$_2^{\bullet-}$)(^{tBu,Tol}DHP$^-$)], respectively, are both supported by planar anionic ligands.[39, 43] The reactivity of the former, [Cu^{II}(η^1-O$_2^{\bullet-}$)(^{iPr2}PCA)]$^-$, is dominated by the high basicity imbued by the dianionic nature of its supporting ligand, (^{iPr2}PCA)$^{2-}$. For instance, this complex reacts with phenols primarily via proton transfer and subsequent electron transfer (i.e., PT/ET).[44] The only exceptions are weakly acidic phenols, which commensurately have weak O-H bonds, where H-atom abstraction is preferred. Additionally, it was reported to react in a nucleophilic manner with acyl halides and to deformylate a selection of electron-rich aldehydes.[45, 46] Conversely, the neutral complex [Cu^{II}(η^1-O$_2^{\bullet-}$)(^{tBu,Tol}DHP$^-$)] performs room temperature catalytic O-atom transfer to PPh$_3$ and dehydrogenation of a variety of readily oxidizable substrates, including 1,2-diphenylhydrazine, benzyl alcohol, and 1,4-dihydroxybenzene.[43] Both [Cu^{II}(η^1-O$_2^{\bullet-}$)(^{iPr2}PCA)]$^-$ and [Cu^{II}(η^1-O$_2^{\bullet-}$)(^{tBu,Tol}DHP$^-$)] show little (or no) reaction with C-H bond substrates. Thus, they are weak oxidants.

In contrast, the complex $[Cu^{II}(\eta^1\text{-}O_2^{\bullet-})(^{X}PPEDC)]^+$ exhibits high electrophilicity, as evidenced by its ability to directly oxidize ferrocenes, perform O-atom transfer to triphenylphosphine, and intramolecularly hydroxylate an *N*-ethylphenyl substituent of the ligand.[40, 47, 48] The latter remains the only published example of C-H bond hydroxylation by a $Cu^{II}(\eta^1\text{-}O_2^{\bullet-})$ complex. Itoh suggested that the comparatively high reactivity of this system is a consequence of its coordination geometry.[49] However, a comparatively small change to the ^{X}PPEDC ligand, involving replacement of its 2-pyridylethyl donor with 2-pyridylmethyl, had a significant impact upon reactivity. The resulting complex $[Cu^{II}(\eta^1\text{-}O_2^{\bullet-})(PPMDC)]^+$ displays greatly reduced electrophilicity and, unlike $[Cu^{II}(\eta^1\text{-}O_2^{\bullet-})(^{X}PPEDC)]^+$, it does not hydroxylate it's *N*-ethylphenyl substituent.[41] Instead, $[Cu^{II}(\eta^1\text{-}O_2^{\bullet-})(PPMDC)]^+$ catalyzes aldol reactivity, which is evidenced to proceed via nucleophilic attack of the carbonyl substrates. A similar catalytic aldol reaction of acetone was also reported by Himmel and co-workers for their complex $[Cu^{II}(\eta^1\text{-}O_2^{\bullet-})(TMGMP)]^+$.[42]

In summary, the small range of published 4-coordinate $Cu^{II}(\eta^1\text{-}O_2^{\bullet-})$ complexes display a broad spectrum of reactivity, both electrophilic and nucleophilic in nature, and it is clear that the supporting ligands have a profound influence upon it. The latter complicates efforts to gain insight by comparison with their more numerous and extensively studied 5-coordinate $Cu^{II}(\eta^1\text{-}O_2^{\bullet-})$ congeners, as they employ ligands possessing very different donors and topological profiles. This led us to target synthesis of a pair of 4- and 5-coordinate $Cu^{II}(\eta^1\text{-}O_2^{\bullet-})$ complexes supported by tridentate and tetradentate ligands, respectively, that differ only in the presence/absence of a single donor. Given our success in stabilizing 5-coordinate $Cu^{II}(\eta^1\text{-}O_2^{\bullet-})$ complexes of tetradentate tris(2-pyridylmethyl)amine (TMPA) ligands by incorporating large aryl substituents onto the 5-position of their pyridine donors,[50] we developed a similarly substituted tridentate bis(2-pyridylmethyl)amine (BPA). The resulting ligand dpb$_2$-^{Me}BPA (**1**) was found to support a $Cu^{II}(\eta^1\text{-}O_2^{\bullet-})$ complex and its reactivity was compared to that of dpb$_3$-TMPA (**2**), which deviates from the former by replacement of one 2-pyridylmethyl arm by a methyl substituent (Chart 1e).

RESULTS AND DISCUSSION

Copper(I) complexes of formulation $[Cu^{I}(\mathbf{1})(NCMe)](X)$, where X = $B(C_6F_5)_4^-$ and SbF_6^-, were prepared by combination of **1** with the corresponding $[Cu^{I}(NCMe)_4](X)$ salts. Oxygenation studies were performed exclusively using $[Cu^{I}(\mathbf{1})(NCMe)][B(C_6F_5)_4]$, but crystals suitable for X-ray crystallographic characterization could only be grown for $[Cu^{I}(\mathbf{1})(NCMe)](SbF_6)$ (Figures 2a and S10, and Table S2). The latter possesses a distorted trigonal pyramidal geometry (as indicated by the geometry index τ_4 = 0.81)[51], with the tertiary amine donor in a pseudo-axial position and Cu-N_{amine}, average Cu-$N_{pyridine}$, and Cu-N_{MeCN} bond distances of 2.206(2), 2.035(2), and 1.891(2) Å, respectively. This is typical for four-coordinate copper(I) complexes of BPA-type ligands that include acetonitrile (MeCN) co-ligands.[26, 28, 29, 52-54]

In contrast, recrystallization of the product obtained from reaction of **1** with the copper(II) salt $Cu^{II}(ClO_4)_2{\cdot}6H_2O$ afforded the square-based pyramidal complex (τ_5 = 0.05)[55] $[Cu^{II}(\mathbf{1})(NCMe)(OH_2)](ClO_4)_2$ (Figures 2b and S11, and Table S3). Therein, N-donors occupy the equatorial positions and a H_2O ligand coordinates in the axial site. As expected for a Jahn-Teller distorted copper(II) complex, the Cu-O distance is comparatively long, at 2.273(13) Å. Consistent with its higher oxidation state, the Cu-N_{amine} and average Cu-$N_{pyridine}$ bond lengths in this complex, 2.016(13) and 1.958(6) Å, respectively, are significantly contracted relative to those of $[Cu^{I}(\mathbf{1})(NCMe)](SbF_6)$. The shortening of the former distance (by approx. 0.19 Å) is particularly large and is likely, partly, due to the accompanying elongation of the Cu-N_{MeCN} distance (by approx. 0.12 Å) to 2.015(13) Å. This increase in Cu-N_{MeCN} bond length can be attributed to reduced π back-bonding in copper(II), relative to copper(I).

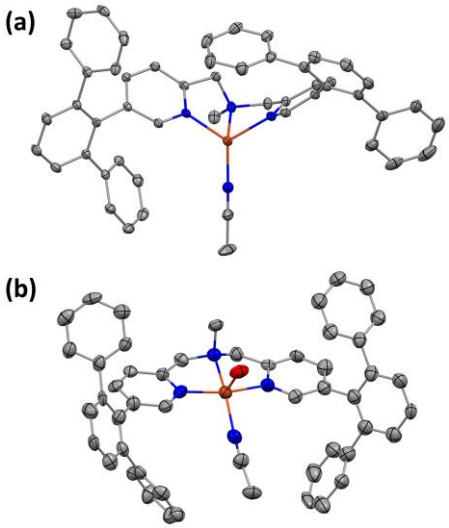

Figure 2. X-ray structures of **(a)** $[Cu^{I}(\mathbf{1})(NCMe)](SbF_6)$ and **(b)** $[Cu^{II}(\mathbf{1})(NCMe)(OH_2)](ClO_4)_2$, depicted using 50% thermal ellipsoids. For clarity, hydrogen atoms, counterions, and solvents molecules have been omitted. Gray, orange, blue, and red spheroids correspond to carbon, copper, nitrogen, and oxygen atoms, respectively.

Cyclic voltammetry measurements for the copper(II) complex $[Cu^{II}(\mathbf{1})(NCMe)(OH_2)](ClO_4)_2$ yielded a quasi-reversible Cu^{II}/Cu^{I} redox couple in acetonitrile solution (Figure S12), with an $E_{1/2}$ value of -0.30 V (*vs* Fc^+/Fc^0). This is more than 100 mV positive of the $E_{1/2}$ recorded for $[Cu^{II}(\mathbf{2})(NCMe)]^{2+}$ (-0.41 V), but it is similar to values reported for $[Cu^{II}$(dtbpb$_3$-TMPA)$(NCMe)]^{2+}$ and $[Cu^{II}(^{Me}BPA)(NCMe)(OTf)]^+$ (-0.32 and -0.29 V, respectively).[50, 56] From this, we can expect $[Cu^{I}(\mathbf{1})(NCMe)]^+$ to have a similar affinity for O_2 binding as $[Cu^{II}$(dtbpb$_3$-TMPA)$]^+$, which displays saturation of O_2 binding in THF solution at ≤ -70°C.

Superoxocopper(II) complex formation and characterization. Bubbling O_2 through pale yellow tetrahydrofuran solutions of $[Cu^{I}(\mathbf{1})(NCMe)][B(C_6F_5)_4]$, at -90 °C (Figure 3a), led to formation of a green species displaying UV-Vis spectral features (λ_{max} = 404 and 722 nm; ε_{max} = 2680 and 1060 M^{-1} cm^{-1}, respectively) characteristic of a $Cu^{II}(\eta^1\text{-}O_2^{\bullet-})$ complex.[22, 23] In contrast to the timeframe of < 10 seconds (s) required for generation of $[Cu^{II}(\eta^1\text{-}O_2^{\bullet-})(\mathbf{2})]^+$, maximum formation of $[Cu^{II}(\eta^1\text{-}O_2^{\bullet-})(\mathbf{1})]^+$ took > 180 s (Figure S14). This difference can be attributed to a divergence in mechanism, with the former involving oxygenation of a copper(I) complex possessing a vacant coordination site (i.e., $[Cu^{I}(\mathbf{2})]^+$) and the latter requiring dissociation of a solvent ligand prior to reaction with O_2. Crucially, the observed $Cu^{II}(\eta^1\text{-}O_2^{\bullet-})$ complex, $[Cu^{II}(\eta^1\text{-}O_2^{\bullet-})(\mathbf{1})]^+$, is stable under the conditions of the experiment, with no evidence for conversion to higher nuclearity **P** or **O** species. Furthermore, warming solutions of $[Cu^{II}(\eta^1\text{-}O_2^{\bullet-})(\mathbf{1})]^+$

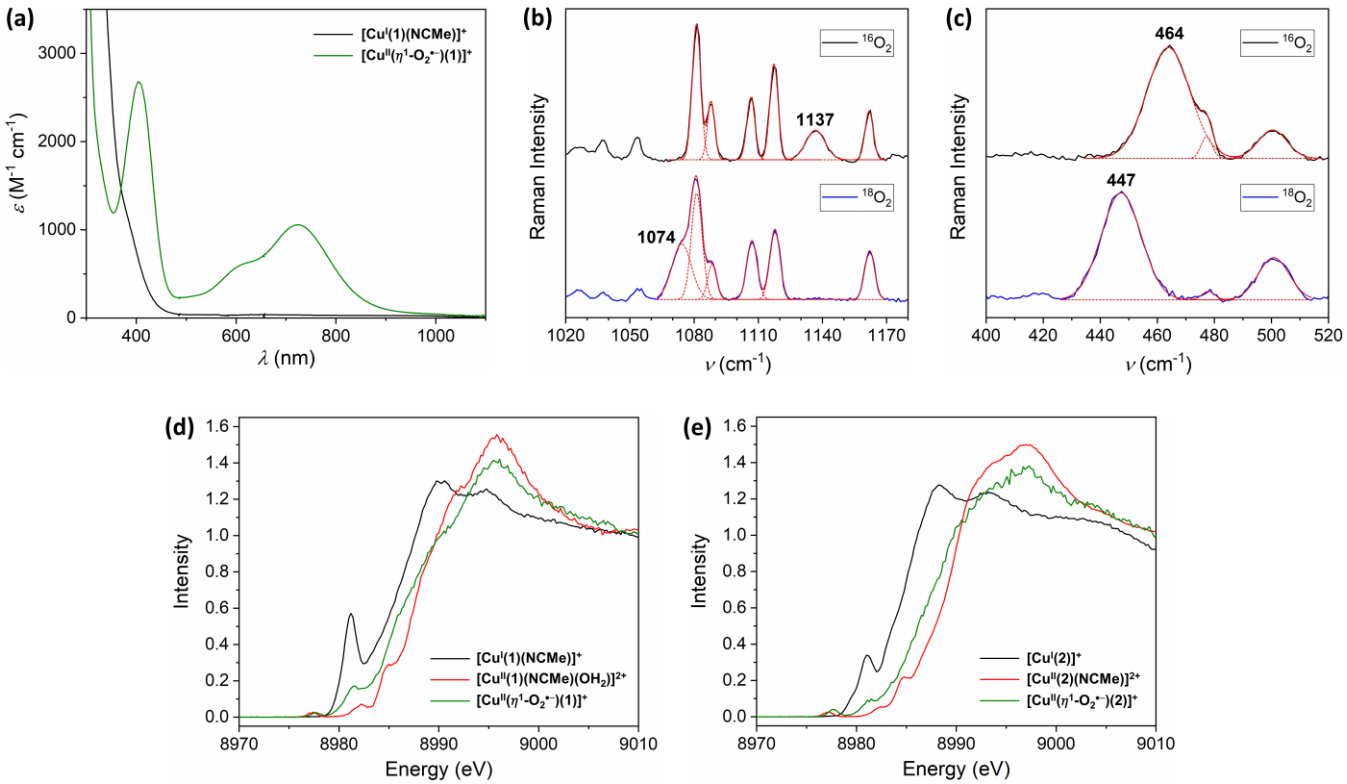

Figure 3. (a) UV-Vis spectra of $[Cu^{I}(\mathbf{1})(NCMe)]^{+}$ and $[Cu^{II}(\eta^{1}\text{-}O_2^{\bullet-})(\mathbf{1})]^{+}$ (black and green lines, respectively), recorded in THF solution at -90°C. Expansions of the **(b)** ν(O-O) and **(c)** ν(Cu-O) containing regions of the resonance Raman spectra of $[Cu^{II}(\eta^{1}\text{-}{}^{16}O_2^{\bullet-})(\mathbf{1})]^{+}$ and $[Cu^{II}(\eta^{1}\text{-}{}^{18}O_2^{\bullet-})(\mathbf{1})]^{+}$ (black and blue lines, respectively), recorded in frozen d_8-THF solution using λ_{ex} = 407 nm. Simulations of the spectra and the Gaussians that comprise them are depicted using solid and dashed red lines, respectively. K-edge HERFD XAS data recorded for **(d)** $[Cu^{I}(\mathbf{1})(NCMe)]^{+}$, $[Cu^{II}(\mathbf{1})(NCMe)(OH_2)]^{2+}$, and $[Cu^{II}(\eta^{1}\text{-}O_2^{\bullet-})(\mathbf{1})]^{+}$ (black, red, and green lines, respectively) and **(e)** $[Cu^{I}(\mathbf{2})]^{+}$, $[Cu^{II}(\mathbf{2})(NCMe)]^{2+}$, and $[Cu^{II}(\eta^{1}\text{-}O_2^{\bullet-})(\mathbf{2})]^{+}$ (black, red, and green lines, respectively).

led to self-decay, but without formation of chromophores characteristic of **P** or **O**.

Confirmation of formation of $[Cu^{II}(\eta^{1}\text{-}O_2^{\bullet-})(\mathbf{1})]^{+}$ was obtained via resonance Raman spectroscopy (Figures 3b and 3c, and S13). Using natural abundance O_2 and an excitation wavelength (λ_{ex}) of 407 nm, peaks at 1137 and 464 cm^{-1} were observed. Production of samples using $^{18}O_2$ gas caused these peaks to shift by 63 and 17 cm^{-1}, respectively, to 1074 and 447 cm^{-1}. Based upon the energies of these peaks and the magnitudes of their isotope shifts, which are very similar to those of previously reported $Cu^{II}(\eta^{1}\text{-}O_2^{\bullet-})$ complexes,[22,23] they can be assigned as O–O and Cu–O stretches, respectively. These ν(O–O) and ν(Cu–O) values are distinct from those of their side-on bound congeners (i.e., $Cu(\eta^{2}\text{-}O_2)$ complexes), which tend to be in the region of ~ 1000 cm^{-1} and 490 – 560 cm^{-1}, respectively.[22]

The electronic structure of $[Cu^{II}(\eta^{1}\text{-}O_2^{\bullet-})(\mathbf{1})]^{+}$ was probed using Cu K-edge HERFD XAS measurements. To provide a frame of reference, data was also collected for $[Cu^{II}(\eta^{1}\text{-}O_2^{\bullet-})(\mathbf{2})]^{+}$, the copper(I) starting complexes $[Cu^{I}(\mathbf{1})(NCMe)]^{+}$ and $[Cu^{I}(\mathbf{2})]^{+}$, and the copper(II) salts $[Cu^{II}(\mathbf{1})(NCMe)(OH_2)]^{2+}$ and $[Cu^{II}(\mathbf{2})(NCMe)]^{2+}$. The spectral features of the series of compounds supported by **1** and **2**, respectively, are broadly similar (Figures 3d and 3e). Both Cu^{I} complexes display an intense feature in the rising edge at ~8981 eV, which is characteristic of Cu^{I} and arises from 1s → 4p transitions. Whereas this appears to be a single and higher intensity feature in $[Cu^{I}(\mathbf{1})(NCMe)]^{+}$, which indicates that all 1s → 4p transitions in this complex occur at similar energies, the corresponding feature in $[Cu^{I}(\mathbf{2})]^{+}$ possesses a shoulder at ~8979 eV. This difference can be attributed to the geometry of $[Cu^{I}(\mathbf{2})]^{+}$ being much closer to a true trigonal pyramid than that of $[Cu^{I}(\mathbf{1})(NCMe)]^{+}$. The geometry of the latter is significantly distorted towards tetrahedral, which will manifest as a reduced energetic separation of the 4p orbitals. Additionally, a trend in white line energy can be seen within both the **1** and **2** ligated series of complexes, with Cu^{II} salts > $Cu^{II}(\eta^{1}\text{-}O_2^{\bullet-})$ > Cu^{I} complexes. This is concordant with expectations, as increasing oxidation state leads to a contraction of core orbitals, thereby increasing the white line energy. The high metal-ligand covalency of the $Cu^{II}(\eta^{1}\text{-}O_2^{\bullet-})$ moiety ameliorates this effect, leading to an intermediate white line energy.

Pre-edge and rising edge features attributable to ligand-to-metal charge transfers (LMCTs) are seen in the XAS spectra of the Cu^{II} salts, $[Cu^{II}(\mathbf{1})(NCMe)(OH_2)]^{2+}$ and $[Cu^{II}(\mathbf{2})(NCMe)]^{2+}$. Although similar, albeit weaker, features are seen for the $Cu^{II}(\eta^{1}\text{-}O_2^{\bullet-})$ complexes, they likely arise from residual Cu^{I} starting materials. More specifically, the XAS spectra of $[Cu^{II}(\eta^{1}\text{-}O_2^{\bullet-})(\mathbf{1})]^{+}$ and $[Cu^{II}(\eta^{1}\text{-}O_2^{\bullet-})(\mathbf{2})]^{+}$, depicted in Figure 3, are estimated to contain contributions from approximately 20% $[Cu^{I}(\mathbf{1})(NCMe)]^{+}$ and 5% $[Cu^{I}(\mathbf{2})]^{+}$, respectively. These impurities prevent any definitive statements regarding the greater intensity observed for the pre-edge of $[Cu^{II}(\eta^{1}\text{-}O_2^{\bullet-})(\mathbf{2})]^{+}$ relative to $[Cu^{II}(\eta^{1}\text{-}O_2^{\bullet-})(\mathbf{1})]^{+}$. However, we can

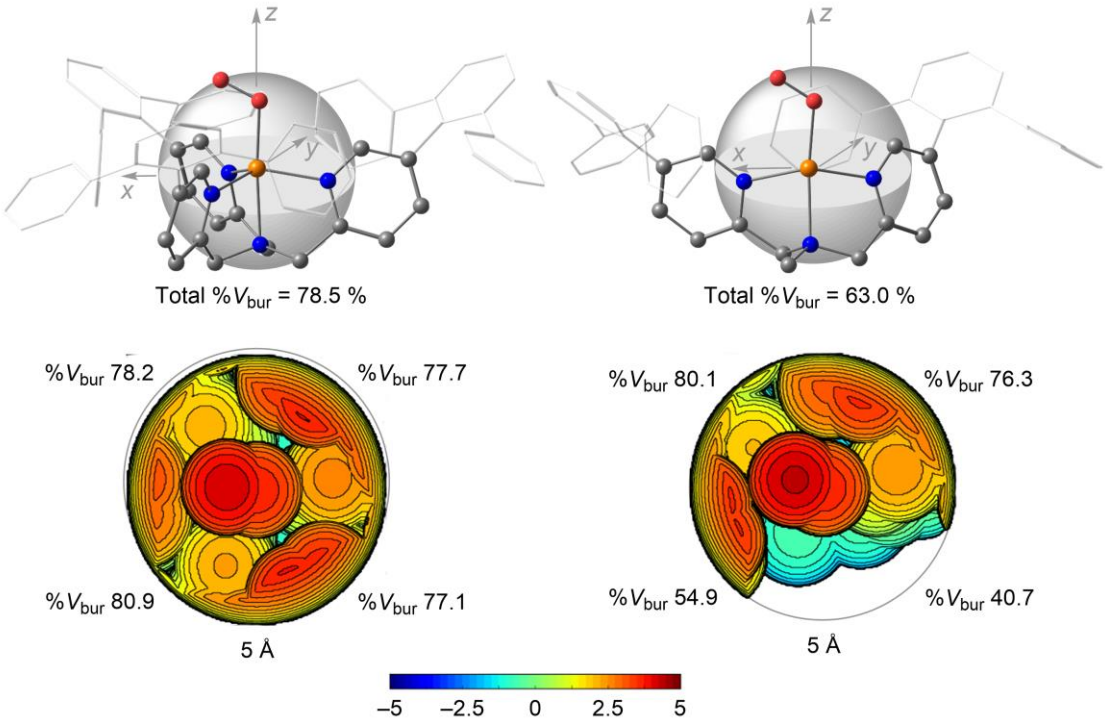

Figure 4. Topographic steric maps of the DFT calculated geometry optimized structures of **(left)** $[Cu^{II}(\eta^1\text{-}O_2^{\bullet-})(\mathbf{2})]^+$ and **(right)** $[Cu^{II}(\eta^1\text{-}O_2^{\bullet-})(\mathbf{2})]^+$, with their Cu-O bonds oriented perpendicular to the plane of the page and pointing towards the viewer. The distance above or below the Cu ions (in Å), which are set as the origin, is color coded according to the figure key.

confidently conclude that the pre-edges intensities and energies of the $Cu^{II}(\eta^1\text{-}O_2^{\bullet-})$ complexes and Cu^{II} salts are markedly similar to one another. Additionally, the positions of the pre-edges of $[Cu^{II}(\eta^1\text{-}O_2^{\bullet-})(\mathbf{1})]^+$ and $[Cu^{II}(\eta^1\text{-}O_2^{\bullet-})(\mathbf{2})]^+$ are both shifted by +0.4 eV relative to those of the corresponding Cu^{II} salts.

DFT calculations support formulation of the title Cu-O_2 adduct as $[Cu^{II}(\eta^1\text{-}O_2^{\bullet-})(\mathbf{1})]^+$. Consistent with previous reports, geometry optimizations revealed that the triplet (S = 1) state was most stable for end-on binding of the superoxo moiety (Figure S30 and Table S13).[39, 47, 57-60] The next most stable state is the open-shell singlet, which is about 10 kcal mol^{-1} higher in energy. Efforts to locate a closed-shell $Cu^{II}(\eta^1\text{-}O_2^{\bullet-})$ structure failed. Similarly, attempts to calculate side-on bound $[Cu(\eta^2\text{-}O_2)(\mathbf{1})]^+$ were also largely unsuccessful. More specifically, a stable wavefunction could not be located for the closed-shell singlet, and geometry optimizations for the open-shell singlet and triplet states of $[Cu(\eta^2\text{-}O_2)(\mathbf{1})]^+$ converged to end-on bound $Cu^{II}(\eta^1\text{-}O_2^{\bullet-})$ structures (Figure S31 and Table S14).

The geometry optimized structure of the lowest energy triplet state calculated for $[Cu^{II}(\eta^1\text{-}O_2^{\bullet-})(\mathbf{1})]^+$ (Figure 4, right) displays a seesaw geometry (τ_4 = 0.42). This contrasts with the distorted trigonal pyramidal geometries of the experimentally observed and calculated structures (both τ_4 = 0.81) of the starting complex $[Cu^{I}(\mathbf{1})(NCMe)]^+$ (Figures 2 and S29), but is similar to the DFT geometry optimized structures of other 4-coordinate $Cu^{II}(\eta^1\text{-}O_2^{\bullet-})$ complexes. The geometry index τ_4 values[51] of $[Cu^{II}(\eta^1\text{-}O_2^{\bullet-})(^{iPr2}PCA)]^-$, $[Cu^{II}(\eta^1\text{-}O_2^{\bullet-})(^{X}PPEDC)]^+$, $[Cu^{II}(\eta^1\text{-}O_2^{\bullet-})(PPMDC)]^+$, $[Cu^{II}(\eta^1\text{-}O_2^{\bullet-})(TMGMP)]^+$, and $[Cu^{II}(^{tBu,Tol}DHP^{2-\bullet})]$ are 0.16, 0.41, 0.36, 0.16, and 0.56, respectively.[39, 41, 43, 61] The lowest energy triplet state of $[Cu^{II}(\eta^1\text{-}O_2^{\bullet-})(\mathbf{1})]^+$ displays a Cu-O-O bond angle and an O-O bond length of 118.8° and 1.253 Å, respectively (Table S13). The latter is short for a superoxo anion. However, the functional B3LYP has a well-documented tendency to overestimate metal-ligand bond lengths, which will reduce the extent of charge transfer into π-acceptor ligands (e.g., O_2). Thus, underestimation of the O-O bond length is expected.

As might be expected, TDDFT calculated UV-Vis spectra for the triplet and open-shell singlet states are, in terms of general appearance, very similar to one another (Figures S38 – S40). Although the experimental spectral features are reasonably well reproduced for both spin states, the relative band intensities in the triplet state better fits experiment. TDDFT calculated XAS spectra yield similar conclusions (Figure S44). Those of the triplet and singlet states of $[Cu^{II}(\eta^1\text{-}O_2^{\bullet-})(\mathbf{1})]^+$ have rising edges that closely resemble one another. However, the calculated XAS spectrum of the triplet state more accurately reproduces the experimentally observed shift in pre-edge energy relative to $[Cu^{II}(\mathbf{1})(NCMe)(OH_2)]^{2+}$ (0.4 eV in both experiment and calculation) and the relative differences to the rising edge energies of $[Cu^{I}(\mathbf{1})(NCMe)]^+$ and $[Cu^{II}(\mathbf{1})(NCMe)(OH_2)]^{2+}$. The reliability of our computational models are validated by the TDDFT calculated XAS spectra of $[Cu^{I}(\mathbf{1})(NCMe)]^+$ and $[Cu^{II}(\mathbf{1})(NCMe)(OH_2)]^{2+}$, which closely reproduce their experimentally observed features. See the Supporting Information for discussion of these results.

To better describe the electronic structure of $[Cu^{II}(\eta^1\text{-}O_2^{\bullet-})(\mathbf{1})]^+$ and more accurately estimate its singlet-triplet energy splitting, multiconfigurational N-electron valence state perturbation theory calculations, based on a (12,12) complete active space reference wave function (CASSCF/NEVPT2), were performed. Active space natural orbitals and their occupation

numbers are provided in the Supporting Information (Figures S36 and S37). As expected, the CASSCF/NEVPT2 calculated triplet state is characterized by a single determinant, with singly occupied $3d_{z^2}$ and π^*_v orbitals and full occupation of the remaining four Cu 3d orbitals (Table S16). In contrast, the singlet wavefunction is comprised of two configurations with weights of 0.63 and 0.34 (Table S17), which indicates that this state possesses high biradical character. These singly occupied orbitals have occupation numbers of 1.318 and 0.681 (Figure S37), respectively, and show more mixing between the Cu $3d_{z^2}$ and O 2p orbitals than the triplet state. The other Cu 3d orbitals are doubly occupied. In essence, the CASSCF calculations yield a $Cu^{II}(\eta^1\text{-}O_2^{\bullet-})$ description displaying either a triplet or singlet diradical state. Whilst DFT predicts that the triplet state is significantly more stable than the open-shell singlet state, CASSCF/NEVPT2 places the former 1.2 kcal mol^{-1} higher in energy than the latter (Tables S18 and S19). Thus, it can be concluded that the two spin states are nearly degenerate. This outcome is consistent with reports made for related systems.[62, 63]

Topographic steric maps of the DFT geometry optimized structures of $[Cu^{II}(\eta^1\text{-}O_2^{\bullet-})(\mathbf{1})]^+$ and $[Cu^{II}(\eta^1\text{-}O_2^{\bullet-})(\mathbf{2})]^+$ (Figures 4 and S34) were generated using the SambVca 2 web tool,[64, 65] which revealed that they possess total buried volumes ($\%V_{bur}$) of 63.0 and 78.5 %, respectively. From visual inspection, it is clear that the steric bulk is fairly evenly distributed around the $Cu^{II}(\eta^1\text{-}O_2^{\bullet-})$ moiety in $[Cu^{II}(\eta^1\text{-}O_2^{\bullet-})(\mathbf{2})]^+$, whereas one face of $[Cu^{II}(\eta^1\text{-}O_2^{\bullet-})(\mathbf{1})]^+$ is comparatively open. This is evident in the $\%V_{bur}$ for the four quadrants of these complexes, with the former showing little variation (77.1 – 80.9 %) and the latter having two quadrants with significantly lower $\%V_{bur}$ of 54.9 and 40.7 % (versus 76.3 and 80.1% of the other two quadrants). On this basis alone, one would expect steric inhibition of reaction with substrates to be significantly reduced in $[Cu^{II}(\eta^1\text{-}O_2^{\bullet-})(\mathbf{1})]^+$ relative to its 5-coordinate congener, $[Cu^{II}(\eta^1\text{-}O_2^{\bullet-})(\mathbf{2})]^+$.

Reaction with substrates. To allow comparison with $[Cu^{II}(\eta^1\text{-}O_2^{\bullet-})(\mathbf{2})]^+$, reaction of $[Cu^{II}(\eta^1\text{-}O_2^{\bullet-})(\mathbf{1})]^+$ with a series of 4-substituted (X) 2,6-di-tert-butylphenols (X-ArOH) was studied at -90°C. In all cases, this proceeded with first order decay of the UV-Vis features associated with the $Cu^{II}(\eta^1\text{-}O_2^{\bullet-})$ unit and growth of two bands centered at around 530 – 590 and 730 – 790 nm (Figures 5a and S15), respectively. The precise spectral features (λ_{max} and ε_{max} values) of the products were found to depend upon the identity of the substituent X. However, the intensities of the two bands suggest that they possess some ligand-to-metal charge transfer (LMCT) character. Additionally, EPR spectra of the products of reaction with X-ArOH (Figure S24) all display signals indicative of a copper(II) complex possessing a $d_{x^2\text{-}y^2}$ ground state (i.e., $g_z > g_x = g_y$). The para substituents (X) of the various X-ArOH substrates did not significantly impact the EPR spectral parameters (Table S5).

Taken together, the aforementioned findings are consistent with formulation of the products of reaction of $[Cu^{II}(\eta^1\text{-}O_2^{\bullet-})(\mathbf{1})]^+$ with X-ArOH as $[Cu^{II}(OAr\text{-}X)(\mathbf{1})]^+$. This notion is supported by the striking similarity of their UV-Vis spectra to those reported for the phenoxocopper(II) complexes $[Cu^{II}(OAr)(^{iPr2}PCA)]^-$ and $[Cu^{II}(OAr)(^{X}PPEDC)]^+$, which were obtained from reaction of the corresponding 4-coordinate superoxocopper(II) complexes, $[Cu^{II}(\eta^1\text{-}O_2^{\bullet-})(^{iPr2}PCA)]^-$ and $[Cu^{II}(\eta^1\text{-}O_2^{\bullet-})(^{X}PPEDC)]^+$, with 4-substituted phenols.[44, 48] In particular, $[Cu^{II}(OAr)(^{iPr2}PCA)]^-$ and $[Cu^{II}(OAr)(^{X}PPEDC)]^+$ both display chromophores comprised of the two moderately intense features at around 490 – 540 and 700 – 740 nm, respectively.

Unfortunately, the $[Cu^{II}(OAr\text{-}X)(\mathbf{1})]^+$ complexes are not thermally stable, which prevented characterization by X-ray crystallography and collection of informative electrospray ionization mass spectrometry (ESI-MS) data. However, independent preparation, by combination of $[Cu^{II}(\mathbf{1})(NCMe)(OH_2)]^{2+}$ with X-ArOK (at -90°C), afforded complexes possessing very similar UV-Vis and EPR spectra (Figures S23 and S25, respectively). Additionally, a DFT exploration of the potential energy surface of 4-coordinate $[Cu^{II}(OAr\text{-}Me)(\mathbf{1})]^+$ revealed three energetically close minima corresponding to different phenoxocopper(II) conformers (Figure S33). All three minima display distorted square planar or seesaw geometries (τ_4 = 0.23 – 0.48; Table S15), near-axial EPR parameters (Table S21), and TDDFT calculated UV-Vis spectra that bear a close resemblance to experiment (Figures S41 – S43), wherein the transitions possess significant LMCT character. These results reaffirm our assignment.

Reaction between $[Cu^{II}(\eta^1\text{-}O_2^{\bullet-})(\mathbf{1})]^+$ and X-ArOH is expected to proceed either via protonation of the superoxo moiety or by a hydrogen atom transfer (HAT) reaction (Scheme S2). Protonation would yield $[Cu^{II}(OAr\text{-}X)(\mathbf{1})]^+$ and $HO_2^{\bullet}$, which would be expected to disproportionate to ½ equiv each of O_2 and H_2O_2. There should be no oxidation of phenol. In contrast, HAT would initially yield hydroperoxocopper(II) complex, $[Cu^{II}(OOH)(\mathbf{1})]^+$, and phenoxyl radical, X-ArO$^{\bullet}$. Subsequent, rapid protonolysis of $[Cu^{II}(OOH)(\mathbf{1})]^+$ by comparatively acidic X-ArOH would provide free H_2O_2 and the experimentally observed $[Cu^{II}(OAr\text{-}X)(\mathbf{1})]^+$. Contrary to expectations for a HAT reaction pathway, formation of X-ArO$^{\bullet}$ was not observed by UV-Vis spectroscopy, and it was detected by EPR spectroscopy in only one case (i.e., MeO-ArO$^{\bullet}$) and in minor quantities (Figure S24a). Although this would seem to preclude a HAT mechanism, the absence of X-ArO$^{\bullet}$ may result from rapid conversion to other products. Similar observations were made by Karlin and co-workers for the complex $[Cu^{II}(\eta^1\text{-}O_2^{\bullet-})(DMM\text{-}TMPA)]^+$, and were rationalized by invocation of a mechanism revolving around reaction of X-ArO$^{\bullet}$ with another molecule of $[Cu^{II}(\eta^1\text{-}O_2^{\bullet-})(DMM\text{-}TMPA)]^+$.[66] An adaptation of this published mechanism, incorporating the observed formation of phenolate complex $[Cu^{II}(OAr\text{-}X)(\mathbf{1})]^+$, is given in Scheme S2. In terms of final products, it is expected to yield 1 equiv each of H_2O_2 and $[Cu^{II}(OAr\text{-}X)(\mathbf{1})]^+$, and ½ equiv of oxidized phenol.

To differentiate between the two aforementioned mechanistic possibilities for reaction of $[Cu^{II}(\eta^1\text{-}O_2^{\bullet-})(\mathbf{1})]^+$ with X-ArOH, analysis of the product mixtures was performed by GC-MS and iodometric titration. For all X-ArOH substrates, this afforded ½ equiv 2,6-di-tert-butyl-1,4-benzoquinone (i.e., approx. 50 % yield; Scheme 1 and Table S8) and 1 equivalent of H_2O_2 (Table S12). The observed reaction stoichiometry is entirely consistent with the postulated HAT mechanism. This differentiates $[Cu^{II}(\eta^1\text{-}O_2^{\bullet-})(\mathbf{1})]^+$ from $[Cu^{II}(\eta^1\text{-}O_2^{\bullet-})(^{iPr2}PCA)]^-$ and $[Cu^{II}(\eta^1\text{-}O_2^{\bullet-})(^{X}PPEDC)]^+$, which both react with phenols via protonolysis of the superoxo ligand.[44, 48] The observed pseudo-first-order rate constants (k_{obs}) derived from reaction with X-ArOH were found to be linearly dependent upon substrate concentration (Figures 5b and S16), thereby yielding second order rate constants (k_2). These values were found to be significantly larger than those measured for the tetradentate ligand coordinated analogues $[Cu^{II}(\eta^1\text{-}O_2^{\bullet-})(tpb_3\text{-}TMPA)]^+$ and $[Cu^{II}(\eta^1\text{-}O_2^{\bullet-})(\mathbf{2})]^+$ (Table S4 and Figure S19).[50] For instance, reaction of $[Cu^{II}(\eta^1\text{-}O_2^{\bullet-})(\mathbf{1})]^+$ and $[Cu^{II}(\eta^1\text{-}O_2^{\bullet-})(\mathbf{2})]^+$

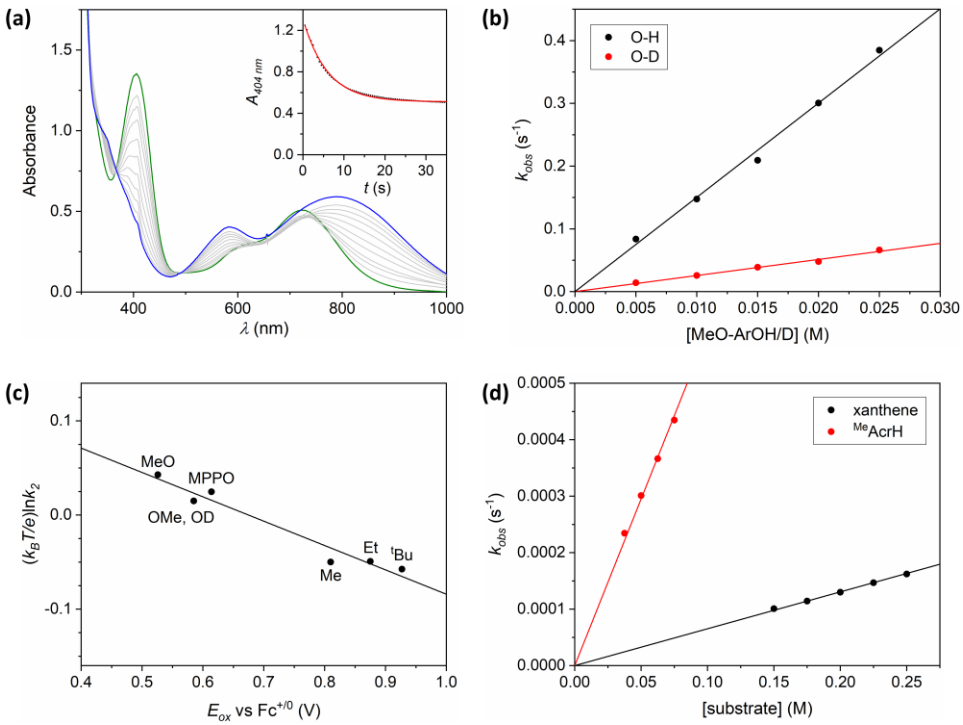

Figure 5. (a) Main: UV-Vis spectral changes observed upon reaction of $[Cu^{II}(\eta^1\text{-}O_2^{\bullet-})(\mathbf{1})]^+$ with 2,6,-di-tert-butyl-4-methoxyphenol (MeO-ArOH). Green, black, and gray lines correspond to $[Cu^{II}(\eta^1\text{-}O_2^{\bullet-})(\mathbf{1})]^+$, the product of reaction, and the spectra recorded in between. Inset: absorbance at 404 nm as a function of time and best-fit line (black dots and red line, respectively). **(b)** A plot of the observed rate constants (k_{obs}, s^{-1}) versus substrate concentration (M), including best-fit lines, recorded for reaction of $[Cu^{II}(\eta^1\text{-}O_2^{\bullet-})(\mathbf{1})]^+$ with MeO-ArOH and MeO-ArOD (black and red circles/ lines, respectively). **(c)** A Markus plot of $(k_BT/e)\ln(k_2)$ values obtained from reaction of $[Cu^{II}(\eta^1\text{-}O_2^{\bullet-})(\mathbf{1})]^+$ with 4-substituted-2,6,-di-tert-butylphenols (X-ArOH) versus the oxidation potentials (E_{ox}, V *vs* Fc^+/Fc^0) of the X-ArOH substrates. **(d)** A plot of the observed rate constants (k_{obs}, s^{-1}) versus substrate concentration (M) recorded for reaction of $[Cu^{II}(\eta^1\text{-}O_2^{\bullet-})(\mathbf{1})]^+$ with *N*-methyl-9,10-dihydroacridine (^{Me}AcrH) and xanthene (black and red circles/ lines, respectively). All reactions depicted were performed in THF solution at -90°C.

with MeO-ArOH (at -90°C) proceeds with k_2 values of 15 and 0.13 M^{-1} s^{-1}, respectively. This corresponds to > 100-fold faster reaction of $[Cu^{II}(\eta^1\text{-}O_2^{\bullet-})(\mathbf{1})]^+$ relative to $[Cu^{II}(\eta^1\text{-}O_2^{\bullet-})(\mathbf{2})]^+$.

To determine whether the difference in oxidative facility of $[Cu^{II}(\eta^1\text{-}O_2^{\bullet-})(\mathbf{1})]^+$ and $[Cu^{II}(\eta^1\text{-}O_2^{\bullet-})(\mathbf{2})]^+$ originates from a change in mechanism, k_2 values for reaction with the deuterated substrate MeO-ArOD were measured (Figures 5b and S21a) and their primary kinetic isotope effects (KIEs) calculated. The KIE of 5.9 obtained for $[Cu^{II}(\eta^1\text{-}O_2^{\bullet-})(\mathbf{1})]^+$ at -90°C is very similar to the value of 5.2 measured for $[Cu^{II}(\eta^1\text{-}O_2^{\bullet-})(\mathbf{2})]^+$ at -40°C, and is suggestive of rate determining H-atom abstraction from the phenolic substrate. To verify this conclusion, a Marcus-type plot of $\log(k_2)$ values obtained from reaction of $[Cu^{II}(\eta^1\text{-}O_2^{\bullet-})(\mathbf{1})]^+$ with a series of X-ArOH substrates versus the oxidation potential (E_{ox}) of the substrates was constructed (Figure 5c). For such a plot, a slope with a gradient of 0 would be expected for a pure HAT reaction, whereas an initial discrete e^- transfer would yield a value between -0.5 and -1.0.[67-69] Conversely, given that the acidity of phenols increases in parallel with their E_{ox} values, a positive slope would be obtained for a reaction involving an initial discrete proton transfer step. The Marcus-type plot for $[Cu^{II}(\eta^1\text{-}O_2^{\bullet-})(\mathbf{1})]^+$ displays a linear correlation possessing a slope of -0.26, which is indicative of a HAT reaction that proceeds via a transition state involving significant charge transfer.[66, 70, 71] This is very similar to the value of -0.24 obtained from an analogous plot for the complex $[Cu^{II}(\eta^1\text{-}O_2^{\bullet-})(tpb_3\text{-}TMPA)]^+$, whose reactivity is essentially identical to $[Cu^{II}(\eta^1\text{-}O_2^{\bullet-})(\mathbf{2})]^+$.[50] In essence, reaction of $[Cu^{II}(\eta^1\text{-}O_2^{\bullet-})(\mathbf{1})]^+$ and $[Cu^{II}(\eta^1\text{-}O_2^{\bullet-})(Ar_3\text{-}TMPA)]^+$ with X-ArOH substrates has the same general mechanistic properties, and, therefore, the difference in the rate at which they react is associated with other factors.

Reaction of $[Cu^{II}(\eta^1\text{-}O_2^{\bullet-})(\mathbf{1})]^+$ with substrates containing weak C-H bonds was also examined, but it presented a more complicated picture. This is because these substrates often possess olefinic functionality, which are able to bind to copper(I). Given that O_2 binding is an equilibrium process, such substrates can cause deoxygenation of $[Cu^{II}(\eta^1\text{-}O_2^{\bullet-})(\mathbf{1})]^+$ and formation of a copper(I) olefin complex, $[Cu^{I}(\mathbf{1})(olefin)]^+$. Behavior of this type was observed for the $[Cu^{II}(\eta^1\text{-}O_2^{\bullet-})(Ar_3\text{-}TMPA)]^+$ complexes,[50] but it is more pronounced in $[Cu^{II}(\eta^1\text{-}O_2^{\bullet-})(\mathbf{1})]^+$. For instance, addition of 10 equiv of 1,4-cyclohexadiene (1,4-CHD) to $[Cu^{II}(\eta^1\text{-}O_2^{\bullet-})(\mathbf{1})]^+$ caused near instantaneous loss of its chromophore and formation of a copper(I) complex (Figure S17b), which is presumed to be $[Cu^{I}(\mathbf{1})(1,4\text{-}CHD)]^+$. This complex can be made independently by addition of 1,4-CHD to a THF solution of $[Cu^{I}(\mathbf{1})(NCMe)]^+$, which caused a change in color from pale yellow to colorless. The UV-Vis spectral change associated with this reaction and the ^{1}H NMR spectrum of the product are provided in the Supporting Information (Figures S5 and S17c).

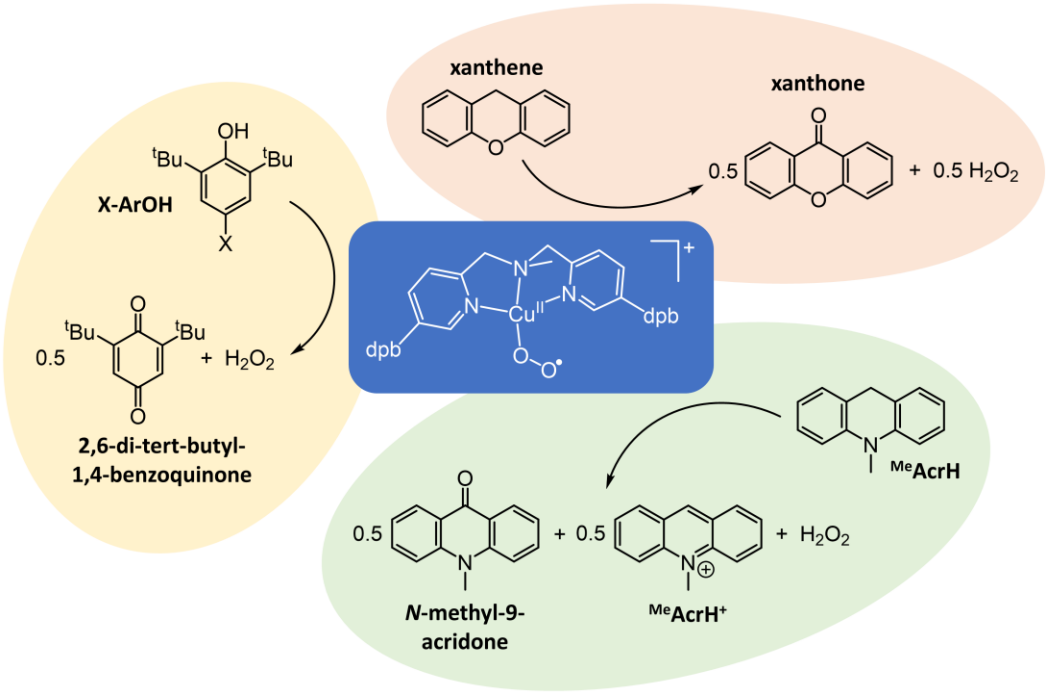

Scheme 1. A summary of the substrates used in the reaction kinetic studies with $[Cu^{II}(\eta^1\text{-}O_2^{\bullet-})(\mathbf{1})]^+$ and the products obtained. Note, in X-ArOH, X = OMe, MPPO, Me, Et, and tBu. MPPO = 2-methyl-1-phenylpropan-2-yloxy.

A similarly fast reaction was observed (Figure S17a) upon addition of 1-benzyl-1,4-dihydronicotinamide (BNAH), in place of 1,4-CHD, to $[Cu^{II}(\eta^1\text{-}O_2^{\bullet-})(\mathbf{1})]^+$. It was initially assumed that this solely reflected dissociation of O_2 and binding of BNAH in its place. However, reaction work-up provided a 41(5) % yield of 1-benzylnicotinamidium (BNA^+; Eqn. S3 and Table S9). This suggests that binding of O_2 and BNAH to the copper(I) centre are both in equilibrium and small concentrations of $[Cu^{II}(\eta^1\text{-}O_2^{\bullet-})(\mathbf{1})]^+$ are present, which rapidly oxidizes BNAH. Given the resulting mechanistic complexity, no efforts were made to deconvolute the kinetic data and, instead, we sought substrates with lower tendencies to bind to copper(I).

The substrates *N*-methyl-9,10-dihydroacridine (^{Me}AcrH) and xanthene were observed to have a minimal impact upon the chromophore of $[Cu^{II}(\eta^1\text{-}O_2^{\bullet-})(\mathbf{1})]^+$ (Figure S18), which implies comparatively weak coordination to copper(I). This allowed for non-ambiguous measurement of reaction kinetics. Reaction of ^{Me}AcrH and xanthene with $[Cu^{II}(\eta^1\text{-}O_2^{\bullet-})(\mathbf{1})]^+$ were found to be first-order in both complex and substrates, thereby yielding k_2 values of 0.0059 and 0.00065 $M^{-1}\ s^{-1}$, respectively (Figure 5d). The ~1 order of magnitude faster reaction with ^{Me}AcrH reflects the smaller C-H bond dissociation enthalpy (BDE) of this substrate relative to that of xanthene (BDEs of 73.0 and 77.9 kcal mol^{-1}, respectively).[72, 73]

EPR spectra of the products obtained from reaction with the C-H bond substrates ^{Me}AcrH and xanthene were near identical (Figure S26 and Table S7), with a single axial signal corresponding to a copper(II) complex possessing a $d_{x^2-y^2}$ ground state (i.e., $g_z > g_x = g_y$). Based upon the following discussion, this is assumed to be a hydroxocopper(II) complex, $[Cu^{II}(OH)(\mathbf{1})]^+$. However, there is a difference in the reaction stoichiometry of these two substrates (Scheme 1). In the case of xanthene, ½ equiv of both xanthone and H_2O_2 were produced (yields of 48(4) and 59(5) %, respectively). This is consistent with a mechanism involving a rate-determining HAT from xanthene, and rapid reaction of the resulting C-based radical with a second molecule of $[Cu^{II}(\eta^1\text{-}O_2^{\bullet-})(\mathbf{1})]^+$ to yield an alkylperoxocopper(II) species (Scheme S3). Heterolytic cleavage of the O-O bond (and H^+ transfer) would afford xanthone and $[Cu^{II}(OH)(\mathbf{1})]^+$. Given the absence of UV-Vis spectroscopic features typical of a hydroperoxocopper(II) complex, it is inferred that the ½ equiv of $[Cu^{II}(OOH)(\mathbf{1})]^+$ produced in the initial HAT reaction is not stable and rapidly decays via hydrolysis to $[Cu^{II}(OH)(\mathbf{1})]^+$, thereby yielding the observed H_2O_2. In support of this notion, we were unable to independently generate a $[Cu^{II}(OOH)(\mathbf{1})]^+$ complex of significant lifetime at -90°C, by treatment of $[Cu^{II}(\mathbf{1})(NCMe)(OH_2)](ClO_4)_2$ with H_2O_2 and triethylamine.

In contrast, reaction with ^{Me}AcrH afforded 1 equiv H_2O_2 and ½ equiv *N*-methyl-9-acridone (respective yields of 90(5) and 49(4) %). At least ½ equiv *N*-methyl-acridinium ($^{Me}Acr^+$) was also produced, but reliable yields proved elusive. The stoichiometric formation of H_2O_2 implies that reaction involves conversion of $[Cu^{II}(\eta^1\text{-}O_2^{\bullet-})(\mathbf{1})]^+$ solely to $[Cu^{II}(OOH)(\mathbf{1})]^+$, which is rapidly hydrolyzed to the EPR detected $[Cu^{II}(OH)(\mathbf{1})]^+$. This can be explained by invocation of the mechanism in Scheme S4. Therein, the *N*-methyl-9-acridinyl radical formed by initial HAT reacts with ½ equiv O_2 to give di(*N*-methyl-9-acridinyl) peroxide. Heterolytic O-O bond cleavage affords the observed ½ equiv each of *N*-methyl-9-acridone and $^{Me}Acr^+$, plus ½ equiv of hydroxide anion. UV-Vis spectral changes support this suggestion. Loss of the chromophore of $[Cu^{II}(\eta^1\text{-}O_2^{\bullet-})(\mathbf{1})]^+$, upon reaction with ^{Me}AcrH, was accompanied by simultaneous formation of bands indicative of formation of $^{Me}Acr^+$ and *N*-methyl-9-acridone (Figures S18a and S22).

Lastly, reaction of $[Cu^{II}(\eta^1\text{-}O_2^{\bullet-})(\mathbf{2})]^+$ with substrates containing weak C-H bonds is difficult to study at -90 °C because it is tremendously slow. Consequently, we have only measured kinetics for these reactions at -40 °C (Figures S20 and S21b). Even at this temperature, $[Cu^{II}(\eta^1\text{-}O_2^{\bullet-})(\mathbf{2})]^+$ displayed

no observable reaction with xanthene, and reaction with BNAH and ^{Me}AcrH proceeded slowly, affording respective k_2 values of 0.14 and 0.00094 M^{-1} s^{-1}. The latter k_2 value is approximately 6 times smaller than that measured for [$Cu^{II}(\eta^1$-$O_2^{\bullet-})$(**1**)]$^+$ at -90 °C. Taking the temperature difference into account, it is estimated that [$Cu^{II}(\eta^1$-$O_2^{\bullet-})$(**1**)]$^+$ reacts with ^{Me}AcrH ~200 times faster than [$Cu^{II}(\eta^1$-$O_2^{\bullet-})$(**2**)]$^+$.

CONCLUSION

In previously published BPA-supported systems, mononuclear Cu-O_2 adducts have been invoked as intermediates in formation of dicopper-O_2 adducts, **P** and **O**. However, they had never been directly observed, which left questions regarding their binding mode, electronic structure, and reactivity properties. Herein, by judicious incorporation of large aryl substituents onto the BPA ligand framework, we have developed a four-coordinate copper(I) complex, [Cu^I(**1**)(NCMe)]$^+$, that binds O_2 to give a superoxocopper(II) complex that is stable against collapse to higher nuclearity **P** or **O** species. This superoxocopper(II) complex was spectroscopically and computationally characterized, and it is concluded that it is end-on bound and is, thusly, formulated as [$Cu^{II}(\eta^1$-$O_2^{\bullet-})$(**1**)]$^+$. There are only a handful of four-coordinate $Cu^{II}(\eta^1$-$O_2^{\bullet-})$ model complexes, with the vast majority reported over the past 30+ years being five-coordinate species. Interestingly, all of these four-coordinate complexes have geometries that are best described as seesaw, with all but one being closer to square planar than tetrahedral.

The ligand design strategy employed in this study was previously used in a series of tetradentate TMPA ligands and allowed us to synthesize a series of highly stable, five-coordinate $Cu^{II}(\eta^1$-$O_2^{\bullet-})$ complexes. This included **2**, which bears the same aryl substituents as **1**. The similarity of these two ligands, which differ by a single pyridine donor, provides a hitherto unavailable opportunity to directly compare the inherent reactivity of four- and five-coordinate $Cu^{II}(\eta^1$-$O_2^{\bullet-})$ species. It was discovered that [$Cu^{II}(\eta^1$-$O_2^{\bullet-})$(**1**)]$^+$ reacts with H-atom donor substrates two orders of magnitude faster than [$Cu^{II}(\eta^1$-$O_2^{\bullet-})$(**2**)]$^+$. More specifically, the former reacts with MeO-ArOH and ^{Me}AcrH approximately 100 and 200 times faster, respectively, than the latter. Based upon topographic steric maps of DFT geometry optimized structures of the two $Cu^{II}(\eta^1$-$O_2^{\bullet-})$ complexes, we attribute this difference to reduced steric hindrance of substrate approach in the four-coordinate complex. However, this does not exclude the possibility of contributions from electronic factors, and we are pursuing further studies intended to probe this. Indeed, there is wide variation between the reactivity of published $Cu^{II}(\eta^1$-$O_2^{\bullet-})$ complexes, with some four-coordinate species displaying greater HAT reactivity than others. This presumably arises from the nature of the supporting ligands, with charge appearing to be a major contributing factor, which implies that ligand design can be used to further enhance/ tune reactivity. Nevertheless, we anticipate our observations of higher reactivity in similarly-ligated four- *vs* five-coordinate $Cu^{II}(\eta^1$-$O_2^{\bullet-})$ complexes will hold true elsewhere. By extension, it is likely no coincidence that four-coordinate $Cu^{II}(\eta^1$-$O_2^{\bullet-})$ intermediates, not their five-coordinate congeners, are believed to be the active oxidants in non-coupled binuclear copper monooxygenases and FGE, where high oxidative capacities are required for hydroxylation of C-H bonds.

ASSOCIATED CONTENT

Supporting Information

The Supporting Information is available free of charge on the ACS Publications website.

Experimental and synthetic procedures, X-ray crystallographic data collection and structural parameters, cyclic voltammetry, additional resonance Raman, XAS, and UV-Vis spectra, reaction kinetics data, and full computational results (PDF).

Accession Codes

CCDC 2284289 and 2284290 contain the supplementary crystallographic data for this paper. These data can be obtained free of charge via www.ccdc.cam.ac.uk/data_request/cif, or by emailing data_request@ccdc.cam.ac.uk, or by contacting The Cambridge Crystallographic Data Centre, 12 Union Road, Cambridge CB2 1EZ, UK; fax: +44 1223 336033.

AUTHOR INFORMATION

Corresponding Author

* Email: serena.debeer@cec.mpg.de
* Email: Tobias.Kraemer@mu.ie
* Email: jengland@lincoln.ac.uk, jaseng197@gmail.com

Author Contributions

‡ S.L. and S.D. contributed equally.

Notes

The authors declare no competing financial interest.

ACKNOWLEDGMENT

JE is grateful to NTU (M4081442, 000416-00001) and the Ministry of Education of Singapore (AcRF Tier 1 grant RG8/19 (S), 002689-00001) for funding. SD thanks the Max Planck Society and the European Research Council (Synergy Grant 856446) for funding. OMS thanks the International Max Planck Society Research School Recharge for funding. We thank Dr. Yongxin Li of the SPMS (NTU) X-ray lab for measurement and refinement of X-ray crystallographic data. In addition, we thank Anchisar Libuda for help with collecting Resonance Raman data. Chris Pollock is thanked for his help as the PIPOXS beamline scientist at Cornell High Energy Synchrotron Source. We acknowledge the DJEI/DES/SFI/HEA Irish Centre for High-End Computing (ICHEC) for the provision of high-performance computing facilities and technical support. TK thanks Dr. Ragnar Bjornsson (CEA Grenoble) for insightful discussions.

REFERENCES

(1) Solomon, E. I.; Heppner, D. E.; Johnston, E. M.; Ginsbach, J. W.; Cirera, J.; Qayyum, M.; Kieber-Emmons, M. T.; Kjaergaard, C. H.; Hadt, R. G.; Tian, L. Copper Active Sites in Biology. *Chem. Rev.* **2014,** *114*, 3659-3853.

(2) Quist, D. A.; Diaz, D. E.; Liu, J. J.; Karlin, K. D. Activation of dioxygen by copper metalloproteins and insights from model complexes. *J. Biol. Inorg. Chem.* **2017**, *22*, 253-288.

(3) Klinman, J. P. The copper-enzyme family of dopamine β-monooxygenase and peptidylglycine α-hydroxylating monooxygenase: Resolving the chemical pathway for substrate hydroxylation. *J. Biol. Chem.* **2006**, *281*, 3013-3016.

(4) Appel, M. J.; Bertozzi, C. R. Formylglycine, a Post-Translationally Generated Residue with Unique Catalytic Capabilities and Biotechnology Applications. *ACS Chem. Biol.* **2015**, *10*, 72-84.

(5) Leisinger, F.; Miarzlou, D. A.; Seebeck, F. P. Non-Coordinative Binding of O_2 at the Active Center of a Copper-Dependent Enzyme. *Angew. Chem. Int. Ed.* **2021**, *60*, 6154-6159.

(6) Appel, M. J.; Meier, K. K.; Lafrance-Vanasse, J.; Lim, H.; Tsai, C.-L.; Hedman, B.; Hodgson, K. O.; Tainer, J. A.; Solomon, E. I.; Bertozzi, C. R. Formylglycine-generating enzyme binds substrate directly at a mononuclear Cu(I) center to initiate O_2 activation. *Proc. Natl. Acad. Sci. U.S.A.* **2019**, *116*, 5370-5375.

(7) Miarzlou, D. A.; Leisinger, F.; Joss, D.; Häussinger, D.; Seebeck, F. P. Structure of formylglycine-generating enzyme in complex with copper and a substrate reveals an acidic pocket for binding and activation of molecular oxygen. *Chem. Sci.* **2019**, *10*, 7049-7058.

(8) Meury, M.; Knop, M.; Seebeck, F. P. Structural Basis for Copper–Oxygen Mediated C–H Bond Activation by the Formylglycine-Generating Enzyme. *Angew. Chem. Int. Ed.* **2017**, *56*, 8115-8119.

(9) Vendelboe, T. V.; Harris, P.; Zhao, Y.; Walter, T. S.; Harlos, K.; El Omari, K.; Christensen, H. E. M. The crystal structure of human dopamine β-hydroxylase at 2.9 Å resolution. *Sci. Adv.* **2016**, *2*, e1500980.

(10) Cowley, R. E.; Tian, L.; Solomon, E. I. Mechanism of O_2 activation and substrate hydroxylation in noncoupled binuclear copper monooxygenases. *Proc. Natl. Acad. Sci. U.S.A.* **2016,** *113*, 12035-12040.

(11) Chen, P.; Solomon, E. I. Oxygen Activation by the Noncoupled Binuclear Copper Site in Peptidylglycine α-Hydroxylating Monooxygenase. Reaction Mechanism and Role of the Noncoupled Nature of the Active Site. *J. Am. Chem. Soc.* **2004**, *126*, 4991-5000.

(12) Prigge, S. T.; Eipper, B. A.; Mains, R. E.; Amzel, L. M. Dioxygen Binds End-On to Mononuclear Copper in a Precatalytic Enzyme Complex. *Science* **2004**, *304*, 864-867.

(13) Schröder, G. C.; O'Dell, W. B.; Webb, S. P.; Agarwal, P. K.; Meilleur, F. Capture of activated dioxygen intermediates at the copper-active site of a lytic polysaccharide monooxygenase. *Chem. Sci.* **2022**, *13*, 13303-13320.

(14) Hagemann, M. M.; Hedegård, E. D. Molecular Mechanism of Substrate Oxidation in Lytic Polysaccharide Monooxygenases: Insight from Theoretical Investigations. *Chem. Eur. J.* **2023**, *29*, e202202379.

(15) Bissaro, B.; Eijsink, Vincent G. H. Lytic polysaccharide monooxygenases: enzymes for controlled and site-specific Fenton-like chemistry. *Essays Biochem.* **2023,** *67*, 575-584.

(16) Forsberg, Z.; Sørlie, M.; Petrović, D.; Courtade, G.; Aachmann, F. L.; Vaaje-Kolstad, G.; Bissaro, B.; Røhr, Å. K.; Eijsink, V. G. H. Polysaccharide degradation by lytic polysaccharide monooxygenases. *Curr. Opin. Struct. Biol.* **2019**, *59*, 54-64.

(17) Wang, B.; Walton, P. H.; Rovira, C. Molecular Mechanisms of Oxygen Activation and Hydrogen Peroxide Formation in Lytic Polysaccharide Monooxygenases. *ACS Catal.* **2019,** *9*, 4958-4969.

(18) Bissaro, B.; Várnai, A.; Røhr Åsmund, K.; Eijsink Vincent, G. H. Oxidoreductases and Reactive Oxygen Species in Conversion of Lignocellulosic Biomass. *Microbiol. Mol. Biol. Rev.* **2018**, *82*, e00029-18.

(19) Tandrup, T.; Frandsen, K. E. H.; Johansen, K. S.; Berrin, J.-G.; Lo Leggio, L. Recent insights into lytic polysaccharide monooxygenases (LPMOs). *Biochem. Soc. Trans.* **2018**, *46*, 1431-1447.

(20) Meier, K. K.; Jones, S. M.; Kaper, T.; Hansson, H.; Koetsier, M. J.; Karkehabadi, S.; Solomon, E. I.; Sandgren, M.; Kelemen, B. Oxygen Activation by Cu LPMOs in Recalcitrant Carbohydrate Polysaccharide Conversion to Monomer Sugars. *Chem. Rev.* **2018**, *118*, 2593-2635.

(21) Kim, B.; Karlin, K. D. Ligand–Copper(I) Primary O_2-Adducts: Design, Characterization, and Biological Significance of Cupric–Superoxides. *Acc. Chem. Res.* **2023**, *56*, 2197-2212.

(22) Elwell, C. E.; Gagnon, N. L.; Neisen, B. D.; Dhar, D.; Spaeth, A. D.; Yee, G. M.; Tolman, W. B. Copper-Oxygen Complexes Revisited: Structures, Spectroscopy, and Reactivity. *Chem. Rev.* **2017**, *117*, 2059-2107.

(23) Mirica, L. M.; Ottenwaelder, X.; Stack, T. D. P. Structure and Spectroscopy of Copper-Dioxygen Complexes. *Chem. Rev.* **2004**, *104*, 1013-1045.

(24) Itoh, S.; Tachi, Y. Structure and O_2-reactivity of copper(I) complexes supported by pyridylalkylamine ligands. *Dalton Trans.* **2006**, 4531-4538.

(25) Osako, T.; Ueno, Y.; Tachi, Y.; Itoh, S. Structures and Redox Reactivities of Copper Complexes of (2-Pyridyl)alkylamine Ligands. Effects of the Alkyl Linker Chain Length. *Inorg. Chem.* **2003**, *42*, 8087-8097.

(26) Lucas, H. R.; Li, L.; Narducci Sarjeant, A. A.; Vance, M. A.; Solomon, E. I.; Karlin, K. D. Toluene and Ethylbenzene Aliphatic C-H Bond Oxidations Initiated by a Dicopper(II)-μ-1,2-Peroxo Complex. *J. Am. Chem. Soc.* **2009**, *131*, 3230-3245.

(27) Tahsini, L.; Kotani, H.; Lee, Y.-M.; Cho, J.; Nam, W.; Karlin, K. D.; Fukuzumi, S. Electron-Transfer Reduction of Dinuclear Copper Peroxo and Bis-μ-oxo Complexes Leading to the Catalytic Four-Electron Reduction of Dioxygen to Water. *Chem. Eur. J.* **2012**, *18*, 1084-1093.

(28) Osako, T.; Terada, S.; Tosha, T.; Nagatomo, S.; Furutachi, H.; Fujinami, S.; Kitagawa, T.; Suzuki, M.; Itoh, S. Structure and dioxygen-reactivity of copper(I) complexes supported by bis(6-methylpyridin-2-ylmethyl)amine tridentate ligands. *Dalton Trans.* **2005**, 3514-3521.

(29) Kunishita, A.; Osako, T.; Tachi, Y.; Teraoka, J.; Itoh, S. Syntheses, structures, and O_2-reactivities of copper(I) complexes with bis(2-pyridylmethyl)amine and bis(2-quinolylmethyl)amine tridentate ligands. *Bull. Chem. Soc. Jpn.* **2006**, *79*, 1729-1741.

(30) Lucas, H. R.; Meyer, G. J.; Karlin, K. D. CO and O_2 Binding to Pseudo-tetradentate Ligand-Copper(I) Complexes with a Variable N-Donor Moiety: Kinetic/Thermodynamic Investigation Reveals Ligand-Induced Changes in Reaction Mechanism. *J. Am. Chem. Soc.* **2010**, *132*, 12927-12940.

(31) Fujisawa, K.; Tanaka, M.; Moro-oka, Y.; Kitajima, N. A Monomeric Side-On Superoxocopper(II) Complex: $Cu(O_2)(HB(3\text{-}tBu\text{-}5\text{-}iPrpz)_3)$. *J. Am. Chem. Soc.* **1994**, *116*, 12079-12080.

(32) Spencer, D. J. E.; Aboelella, N. W.; Reynolds, A. M.; Holland, P. L.; Tolman, W. B. β-Diketiminate Ligand Backbone Structural Effects on $Cu(I)/O_2$ Reactivity: Unique Copper-Superoxo and Bis(μ-oxo) Complexes. *J. Am. Chem. Soc.* **2002**, *124*, 2108-2109.

(33) Aboelella, N. W.; Lewis, E. A.; Reynolds, A. M.; Brennessel, W. W.; Cramer, C. J.; Tolman, W. B. Snapshots of Dioxygen Activation by Copper: The Structure of a 1:1 Cu/O_2 Adduct and Its Use in Syntheses of Asymmetric Bis(μ-oxo) Complexes. *J. Am. Chem. Soc.* **2002**, *124*, 10660-10661.

(34) Reynolds, A. M.; Gherman, B. F.; Cramer, C. J.; Tolman, W. B. Characterization of a 1:1 Cu-O_2 Adduct Supported by an Anilido Imine Ligand. *Inorg. Chem.* **2005**, *44*, 6989-6997.

(35) Iovan, D. A.; Wrobel, A. T.; McClelland, A. A.; Scharf, A. B.; Edouard, G. A.; Betley, T. A. Reactivity of a stable copper–dioxygen complex. *Chem. Commun.* **2017**, *53*, 10306-10309.

(36) Carsch, K. M.; Iliescu, A.; McGillicuddy, R. D.; Mason, J. A.; Betley, T. A. Reversible Scavenging of Dioxygen from Air by a Copper Complex. *J. Am. Chem. Soc.* **2021**, *143*, 18346-18352.

(37) Sarangi, R.; Aboelella, N.; Fujisawa, K.; Tolman, W. B.; Hedman, B.; Hodgson, K. O.; Solomon, E. I. X-ray Absorption Edge Spectroscopy and Computational Studies on $LCuO_2$ Species: Superoxide-Cu^{II} versus Peroxide-Cu^{III} Bonding. *J. Am. Chem. Soc.* **2006**, *128*, 8286-8296.

(38) Aboelella, N. W.; Kryatov, S. V.; Gherman, B. F.; Brennessel, W. W.; Young, V. G., Jr.; Sarangi, R.; Rybak-Akimova, E. V.; Hodgson, K. O.; Hedman, B.; Solomon, E. I.; Cramer, C. J.; Tolman, W. B. Dioxygen Activation at a Single Copper Site: Structure, Bonding, and Mechanism of Formation of 1:1 Cu-O_2 Adducts. *J. Am. Chem. Soc.* **2004**, *126*, 16896-16911.

(39) Donoghue, P. J.; Gupta, A. K.; Boyce, D. W.; Cramer, C. J.; Tolman, W. B. An Anionic, Tetragonal Copper(II) Superoxide Complex. *J. Am. Chem. Soc.* **2010**, *132*, 15869-15871.

(40) Kunishita, A.; Kubo, M.; Sugimoto, H.; Ogura, T.; Sato, K.; Takui, T.; Itoh, S. Mononuclear Copper(II)-Superoxo Complexes that Mimic the Structure and Reactivity of the Active Centers of PHM and DβM. *J. Am. Chem. Soc.* **2009,** *131*, 2788-2789.

(41) Abe, T.; Hori, Y.; Shiota, Y.; Ohta, T.; Morimoto, Y.; Sugimoto, H.; Ogura, T.; Yoshizawa, K.; Itoh, S. Cupric-superoxide complex that induces a catalytic aldol reaction-type C–C bond formation. *Commun. Chem.* **2019,** *2*, 12.

(42) Schön, F.; Biebl, F.; Greb, L.; Leingang, S.; Grimm-Lebsanft, B.; Teubner, M.; Buchenau, S.; Kaifer, E.; Rübhausen, M. A.; Himmel, H.-J. On the Metal Cooperativity in a Dinuclear Copper–Guanidine Complex for Aliphatic C–H Bond Cleavage by Dioxygen. *Chem. Eur. J.* **2019,** *25*, 11257-11268.

(43) Czaikowski, M. E.; McNeece, A. J.; Boyn, J.-N.; Jesse, K. A.; Anferov, S. W.; Filatov, A. S.; Mazziotti, D. A.; Anderson, J. S. Generation and Aerobic Oxidative Catalysis of a Cu(II) Superoxo Complex Supported by a Redox-Active Ligand. *J. Am. Chem. Soc.* **2022**, *144*, 15569-15580.

(44) Bailey, W. D.; Dhar, D.; Cramblitt, A. C.; Tolman, W. B. Mechanistic Dichotomy in Proton-Coupled Electron-Transfer Reactions of Phenols with a Copper Superoxide Complex. *J. Am. Chem. Soc.* **2019**, *141*, 5470-5480.

(45) Bailey, W. D.; Gagnon, N. L.; Elwell, C. E.; Cramblitt, A. C.; Bouchey, C. J.; Tolman, W. B. Revisiting the Synthesis and Nucleophilic Reactivity of an Anionic Copper Superoxide Complex. *Inorg. Chem.* **2019**, *58*, 4706-4711.

(46) Pirovano, P.; Magherusan, A. M.; McGlynn, C.; Ure, A.; Lynes, A.; McDonald, A. R. Nucleophilic Reactivity of a Copper(II)-Superoxide Complex. *Angew. Chem., Int. Ed.* **2014**, *53*, 5946-5950.

(47) Kunishita, A.; Ertem, M. Z.; Okubo, Y.; Tano, T.; Sugimoto, H.; Ohkubo, K.; Fujieda, N.; Fukuzumi, S.; Cramer, C. J.; Itoh, S. Active Site Models for the CuA Site of Peptidylglycine α-Hydroxylating Monooxygenase and Dopamine β-Monooxygenase. *Inorg. Chem.* **2012**, *51*, 9465-9480.

(48) Tano, T.; Okubo, Y.; Kunishita, A.; Kubo, M.; Sugimoto, H.; Fujieda, N.; Ogura, T.; Itoh, S. Redox Properties of a Mononuclear Copper(II)-Superoxide Complex. *Inorg. Chem.* **2013**, *52*, 10431-10437.

(49) Itoh, S. Developing Mononuclear Copper-Active-Oxygen Complexes Relevant to Reactive Intermediates of Biological Oxidation Reactions. *Acc. Chem. Res.* **2015**, *48*, 2066-2074.

(50) Quek, S. Y.; Debnath, S.; Laxmi, S.; van Gastel, M.; Krämer, T.; England, J. Sterically Stabilized End-On Superoxocopper(II) Complexes and Mechanistic Insights into Their Reactivity with O–H, N–H, and C–H Substrates. *J. Am. Chem. Soc.* **2021**, *143*, 19731-19747.

(51) Yang, L.; Powell, D. R.; Houser, R. P. Structural variation in copper(i) complexes with pyridylmethylamide ligands: structural analysis with a new four-coordinate geometry index, τ_4. *Dalton Trans.* **2007**, 955-964.

(52) Shimazaki, Y.; Yokoyama, H.; Yamauchi, O. Copper(I) Complexes with a Proximal Aromatic Ring: Novel Copper–Indole Bonding. *Angew. Chem. Int. Ed.* **1999**, *38*, 2401-2403.

(53) Lionetti, D.; Day, M. W.; Agapie, T. Metal-templated ligand architectures for trinuclear chemistry: tricopper complexes and their O_2 reactivity. *Chem. Sci.* **2013**, *4*, 785-790.

(54) Li, S. T.; Braun-Cula, B.; Hoof, S.; Dürr, M.; Ivanović-Burmazović, I.; Limberg, C. Ligands with Two Different Binding Sites and O_2 Reactivity of their Copper(I) Complexes. *Eur. J. Inorg. Chem.* **2016**, 4017-4027.

(55) Addison, A. W.; Rao, T. N.; Reedijk, J.; van Rijn, J.; Verschoor, G. C. Synthesis, structure, and spectroscopic properties of copper(II) compounds containing nitrogen–sulphur donor ligands; the crystal and molecular structure of aqua[1,7-bis(N-methylbenzimidazol-2′-yl)-2,6-dithiaheptane]copper(II) perchlorate. *J. Chem. Soc., Dalton Trans.* **1984**, 1349-1356.

(56) Ribelli, T. G.; Wahidur Rahaman, S. M.; Krys, P.; Matyjaszewski, K.; Poli, R. Effect of Ligand Structure on the Cu^{II}–R OMRP Dormant Species and Its Consequences for Catalytic Radical Termination in ATRP. *Macromolecules* **2016**, *49*, 7749-7757.

(57) Lanci, M. P.; Smirnov, V. V.; Cramer, C. J.; Gauchenova, E. V.; Sundermeyer, J.; Roth, J. P. Isotopic Probing of Molecular Oxygen Activation at Copper(I) Sites. *J. Am. Chem. Soc.* **2007**, *129*, 14697-14709.

(58) Woertink, J. S.; Tian, L.; Maiti, D.; Lucas, H. R.; Himes, R. A.; Karlin, K. D.; Neese, F.; Wurtele, C.; Holthausen, M. C.; Bill, E.; Sundermeyer, J.; Schindler, S.; Solomon, E. I. Spectroscopic and Computational Studies of an End-on Bound Superoxo-Cu(II) Complex: Geometric and Electronic Factors That Determine the Ground State. *Inorg. Chem.* **2010**, *49*, 9450-9459.

(59) Bhadra, M.; Transue, W. J.; Lim, H.; Cowley, R. E.; Lee, J. Y. C.; Siegler, M. A.; Josephs, P.; Henkel, G.; Lerch, M.; Schindler, S.; Neuba, A.; Hodgson, K. O.; Hedman, B.; Solomon, E. I.; Karlin, K. D. A Thioether-Ligated Cupric Superoxide Model with Hydrogen Atom Abstraction Reactivity. *J. Am. Chem. Soc.* **2021**, *143*, 3707-3713.

(60) Peterson, R. L.; Himes, R. A.; Kotani, H.; Suenobu, T.; Tian, L.; Siegler, M. A.; Solomon, E. I.; Fukuzumi, S.; Karlin, K. D. Cupric Superoxo-Mediated Intermolecular C-H Activation Chemistry. *J. Am. Chem. Soc.* **2011**, *133*, 1702-1705.

(61) No atomic coordinates were provided in reference 42 for the DFT geometry optimized structure of $[Cu^{II}(\eta^1\text{-}O_2^{\bullet-})(TMGMP)]^+$, so it was recalculated herein (Figure S32).

(62) Huber, S. M.; Moughal Shahi, A. R.; Aquilante, F.; Cramer, C. J.; Gagliardi, L. What Active Space Adequately Describes Oxygen Activation by a Late Transition Metal? CASPT2 and RASPT2 Applied to Intermediates from the Reaction of O_2 with a Cu(I)-α-Ketocarboxylate. *J. Chem. Theory Comput.* **2009**, *5*, 2967-2976.

(63) Larsson, E. D.; Dong, G.; Veryazov, V.; Ryde, U.; Hedegård, E. D. Is density functional theory accurate for lytic polysaccharide monooxygenase enzymes? *Dalton Trans.* **2020**, *49*, 1501-1512.

(64) Falivene, L.; Credendino, R.; Poater, A.; Petta, A.; Serra, L.; Oliva, R.; Scarano, V.; Cavallo, L. SambVca 2. A Web Tool for Analyzing Catalytic Pockets with Topographic Steric Maps. *Organometallics* **2016**, *35*, 2286-2293.

(65) Poater, A.; Ragone, F.; Mariz, R.; Dorta, R.; Cavallo, L. Comparing the Enantioselective Power of Steric and Electrostatic Effects in Transition-Metal-Catalyzed Asymmetric Synthesis. *Chem. Eur. J.* **2010**, *16*, 14348-14353.

(66) Lee, J. Y.; Peterson, R. L.; Ohkubo, K.; Garcia-Bosch, I.; Himes, R. A.; Woertink, J.; Moore, C. D.; Solomon, E. I.; Fukuzumi, S.; Karlin, K. D. Mechanistic Insights into the Oxidation of Substituted Phenols via Hydrogen Atom Abstraction by a Cupric-Superoxo Complex. *J. Am. Chem. Soc.* **2014,** *136*, 9925-9937.

(67) Ram, M. S.; Hupp, J. T. Linear free energy relations for multielectron transfer kinetics: a brief look at the Broensted/Tafel analogy. *J. Phys. Chem.* **1990**, *94*, 2378-2380.

(68) Weatherly, S. C.; Yang, I. V.; Thorp, H. H. Proton-Coupled Electron Transfer in Duplex DNA: Driving Force Dependence and Isotope Effects on Electrocatalytic Oxidation of Guanine. *J. Am. Chem. Soc.* **2001**, *123*, 1236-1237.

(69) Osako, T.; Ohkubo, K.; Taki, M.; Tachi, Y.; Fukuzumi, S.; Itoh, S. Oxidation mechanism of phenols by dicopper-dioxygen (Cu_2/O_2) complexes. *J. Am. Chem. Soc.* **2003**, *125*, 11027-11033.

(70) Guttenplan, J. B.; Cohen, S. G. Triplet energies, reduction potentials, and ionization potentials in carbonyl-donor partial charge-transfer interactions. I. *J. Am. Chem. Soc.* **1972**, *94*, 4040-4042.

(71) Wagner, P. J.; Lam, H. M. H. Charge-transfer quenching of triplet .alpha.-trifluoroacetophenones. *J. Am. Chem. Soc.* **1980**, *102*, 4167-4172.

(72) Zhu, X.-Q.; Zhang, M.-T.; Yu, A.; Wang, C.-H.; Cheng, J.-P. Hydride, Hydrogen Atom, Proton, and Electron Transfer Driving Forces of Various Five-Membered Heterocyclic Organic Hydrides

and Their Reaction Intermediates in Acetonitrile. *J. Am. Chem. Soc.* **2008**, *130*, 2501-2516.

(73) Warren, J. J.; Tronic, T. A.; Mayer, J. M. Thermochemistry of Proton-Coupled Electron Transfer Reagents and its Implications. *Chem. Rev.* **2010**, *110*, 6961-7001.